Front. Mech. Eng. 2017, 12(4): 581–590
DOI 10.1007/s11465-017-0454-x

RESEARCH ARTICLE

Biyun LING, Yu WANG, Chunrong PENG, Bing LI, Zhaozhi CHU, Bin LI, Shanhong XIA

Single-chip 3D electric field microsensor

Abstract This paper presents a single-chip 3D electric field microsensor, in which a sensing element is set at the center to detect the *Z*-axis component of an electrostatic field. Two pairs of sensing elements with the same structure are arranged in a cross-like configuration to measure the *X*- and *Y*-axis electrostatic field components. An in-plane rotary mechanism is used in the microsensor to detect the *X*-, *Y*-, and *Z*-axis electrostatic field components simultaneously. The proposed microsensor is compact and presents high integration. The microsensor is fabricated through a MetalMUMPS process. Experimental results show that in the range of 0–50 kV/m, the linearity errors of the microsensor are within 5.5%, and the total measurement errors of the three electrostatic field components are less than 14.04%.

Keywords electric field microsensor, three-dimensional, single-chip, in-plane rotation

1 Introduction

Electrostatic field measurement is crucial in many industrial and scientific areas, such as high voltage direct current (HVDC) power system monitoring [1], lightning hazard warning [2,3], and space plasma studies [4,5]. Consequently, sensors that can accurately detect and quantify electrostatic fields in natural and artificial environments are in demand. Various sensors that can measure electrostatic fields have been developed, and most of them can be classified into four categories, namely, double probes [6], field mills [1,7], optical sensors [8–10], and micromachined electric field sensors (MEFSs) [11–20]. Double probes and field mills are fabricated through traditional machining methods; as a result, they possess large volumes and complex structures and entail high power costs. Optical sensors are based on electro-optic effect or fiber and demonstrate excellent sensitivity; however, they suffer from complicated measurement systems [21], phase bias, and temperature stability problems [22]. Currently, Various MEFSs have been proposed due to the rapid development of micromachining technology. MEFSs possess intrinsic advantages of low power cost, compact size, and batch producibility. MEFSs are based on the principle of charge induction. An alternating charge is induced by periodically changing the electrostatic field on the surface of the sensing electrodes, and the alternating current (AC) with respect to the strength of the electrostatic field around the sensors can be measured.

Most reported MEFSs are single-axis ones, so they cannot measure all three Cartesian components of an electrostatic field. The atmospheric electric field near the surface of the Earth is perpendicular to the ground. However, unlike this electric field, the electrostatic field in several cases (e.g., under HVDC transmission lines [1] and in the ionosphere [4,5]) has an unknown direction before measurement. Therefore, measuring 3D electrostatic fields is indispensable. Wang et al. [20] introduced a biaxial MEFS that can sense an in-plane electrostatic field but has no axis to sense the vertical component; the author asserted that monolithic 2D or 3D MEFSs require high structural integrity and an accurate decoupling calibration method. By deriving a coupling sensitivity matrix, Wen et al. [23] and Fang et al. [24] distributed three 1D MEFSs in-plane and orthogonally to measure a 3D electrostatic field. In their studies, the elimination of coupling interference among the three components of the electrostatic field simply relied on an algorithm instead of the structural design. Although their proposed devices are larger than single-chip MEFSs, their methods can be easily implemented and are minimally restrictive.

To address the need for 3D electrostatic field measurement, this study proposes a single-chip 3D electric field microsensor, in which three orthogonal sensing axes are

Received November 17, 2016; accepted March 20, 2017

Biyun LING, Yu WANG, Chunrong PENG, Bing LI, Zhaozhi CHU, Bin LI, Shanhong XIA (✉)
State Key Laboratory of Transducer Technology, Institute of Electronics, Chinese Academy of Sciences, Beijing 100190, China
Email: shxia@mail.ie.ac.cn

Biyun LING, Yu WANG, Bing LI, Zhaozhi CHU, Bin LI
University of Chinese Academy of Sciences, Beijing 100049, China

placed in one chip. An in-plane rotary mechanism is adopted in the microsensor to detect *X*-, *Y*-, and *Z*-axis electrostatic field components simultaneously. The 3D electric field microsensor is compact and presents high integration.

The structure of this paper is as follows. Section 1 provides a brief introduction to the need for 3D MEFS and presents related studies. Section 2 describes the proposed single-chip 3D electric field microsensor. Section 3 discusses the capability of the proposed microsensor to measure 3D electrostatic fields and the optimization of electrodes through finite element analysis (FEA). Section 4 presents the fabrication process. Experiments are conducted in Section 5 to characterize the 3D electric field microsensor.

2 Working principle and structure

Electrostatically actuated MEFSs can be classified into two categories according to the placement of the sensing and shielding electrodes. The first is vertical MEFS, in which sensing electrodes are patterned over an insulating layer on the substrate beneath the grounded shutter-like shielding electrodes. The second category is lateral MEFS, in which grounded shielding and sensing electrodes are fabricated on the same plane. Compared with lateral MEFS, vertical MEFS has a smaller conversion gain because of its fringe fields at the sidewalls. Therefore, a lateral MEFS-based design was used in this study.

A schematic of the proposed 3D electric field microsensor is shown in Fig. 1. The structures of the device can be classified as fixed or movable. The fixed structures include all strip-type sensing and fixed driving electrodes. The movable structures make up the in-plane rotating structure, which is composed of all strip-type shielding electrodes, movable driving electrodes, and four serpentine springs. The strip-type sensing and strip-type shielding electrodes constitute the sensing elements. The fixed and movable driving electrodes use angular driving comb fingers and work together as push-pull comb drives.

Three orthogonal sensing axes are placed in one chip. The *Z* sensing element is set at the center to detect the *Z*-axis component of the electrostatic field. Two pairs of sensing elements [$(X+, X-)$ and $(Y+, Y-)$] with the same structure are arranged in a cross-like pattern around the *Z* sensing element. In the radial direction, the *Z* sensing element is connected to four symmetrical serpentine springs, whose other ends are fixed to the anchors. These four serpentine springs are used to support the in-plane rotating structure and to achieve large rotation, as demonstrated in previous studies [25]. The push-pull comb drives are located between two adjacent springs. When the in-plane rotation is excited by the push-pull comb drives, the strip-type shielding electrodes oscillate back and forth and cover the sidewalls of the strip-type sensing electrodes.

Electrodes are equipotential on the condition of electrostatic equilibrium, which leads to the distortion of the nearby electric field. Regardless of whether the external electric field is along the radial direction or perpendicular to the plane, an electric field can be generated on the surfaces of the sensing electrodes and is always normal to the surfaces, including the sidewalls, in an inward or outward direction. Therefore, the strength of the electric field on the sidewall changes, and alternating current is produced by periodically covering the sidewalls of the sensing electrodes. The output alternating current, i_s, is defined as

$$i_s = \varepsilon_0 E_n \frac{dA}{dt}, \tag{1}$$

where ε_0 is the permittivity of free space, E_n is the component of the electric field normal to the sensing electrodes, and A is the effective area of the sensing electrodes. The measurements of the *X*- and *Y*-axis electrostatic field components are based on the strength of the distorted electric field in the $X+$, $X-$, $Y+$, and $Y-$

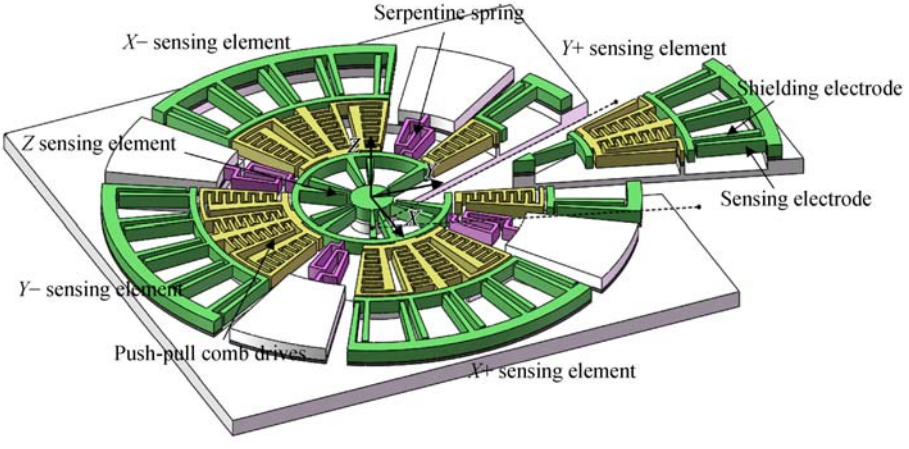

Fig. 1 Schematic of the 3D electric field microsensor

sensing elements. The differential output of the $X+$ and $X-$ sensing elements is used to represent the X-axis component of the electrostatic field, and the differential output of the $Y+$ and $Y-$ sensing elements is used to represent the Y-axis component.

3 Modeling of the 3D electric field microsensor

A modeling analysis was conducted to investigate the capability of the proposed microsensor in 3D electrostatic field measurement. The microsensor structure is complex; thus, a simplified microsensor model, in which all the electrodes are omitted, was initially adopted in a simulation to study the microsensor response to a 3D electrostatic field. The parameters of the electrodes were subsequently optimized to increase the output of the microsensor. Finally, the resonant frequency of the in-plane rotation mode was obtained through a simulation.

3.1 Modeling of 3D electrostatic field measurement

Figure 2 illustrates the simulation model for the response of the proposed microsensor to a 3D electrostatic field with different directions. Five sensing elements were simplified based on theirs outlines, and all the electrodes were disregarded. The Z sensing element was simplified into an annular plate located at the center, and the $X+$, $X-$, $Y+$, and $Y-$ sensing elements were all annular sector plates forming a cross-like configuration around the Z sensing element. All five simplified sensing elements were coaxially placed. In addition, the push-pull comb drives and serpentine springs were disregarded. An electrostatic field with a strength of E_0 was applied. The angle between the electrostatic field and the Z-axis was θ. The angle between the projection of the electrostatic field on the X-Y plane and X-axis was φ. Therefore,

$$E_x = -E_0 \sin\theta \cos\varphi, \tag{2}$$

$$E_y = -E_0 \sin\theta \sin\varphi, \tag{3}$$

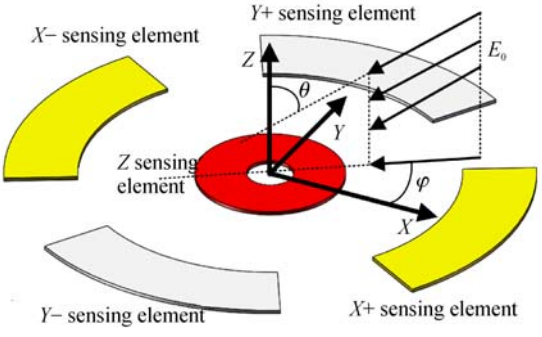

Fig. 2 Simulation model for the response of the proposed microsensor to a 3D electrostatic field with different directions

$$E_z = -E_0 \cos\theta, \tag{4}$$

where E_x, E_y, and E_z are the X-, Y-, and Z-axis components of the electrostatic field, respectively. Q_{x+}, Q_{x-}, Q_{y+}, Q_{y-}, and Q_z are the induced charges on the upper surfaces of the five sensing elements.

$$Q_x = Q_{x+} - Q_{x-}, \tag{5}$$

$$Q_y = Q_{y+} - Q_{y-}, \tag{6}$$

where Q_x is the differential output of the X-axis sensing component and Q_y is the differential output of the Y-axis sensing component. The characteristics of Q_x, Q_y, and Q_z with respect to θ and φ should be similar to those of E_x, E_y, and E_z, respectively, to measure the 3D electrostatic field accurately.

A simulation analysis was conducted with the FEA method. The boundary conditions for the simulation strictly follow calibration. Firstly, a sufficiently large rectangular free space was created. In this free space, the simplified microsensor was placed at the center. Two opposite sides were selected, and opposite voltages were applied to generate a uniform electrostatic field. An electrostatic field from different directions was generated by rotating the rectangular free space. Second, the five simplified elements were all grounded in the simulation because the potentials of all the sensing and shielding electrodes were set to zero in the testing circuit. E_0 was set to 10 V/m. Q_x, Q_y, and Q_z were calculated when the direction of the applied electrostatic field changed circumferentially. As shown in Fig. 3(a), when θ was fixed, the curves of Q_x and Q_y showed good sinusoidal characteristics with a 90° phase difference, whereas Q_z did not change. The curves were in accordance with E_x, E_y, and E_z. As shown in Fig. 3(b), when φ was fixed, Q_x, Q_y, and Q_z versus θ were quarter-sine curves, which agreed well with E_x, E_y, and E_z, respectively. The simulation results demonstrated that the characteristics of Q_x, Q_y, and Q_z with respect to θ and φ were similar to those of E_x, E_y, and E_z, respectively. Therefore, the proposed 3D electric field microsensor can measure 3D electrostatic fields accurately.

However, the magnitude of Q_z is much lower than that of Q_x and Q_y because of the differences in the sensing areas and numbers of sensing elements; thus, Q_x, Q_y, and Q_z cannot represent the applied electrostatic field directly without introducing sensitivity factors. Furthermore, in 3D electrostatic field measurement, coupling interference among the three components of the electrostatic field is unavoidable. Therefore, a sensitivity matrix was employed to compensate for these differences and for decoupling. The sensitivity matrix is discussed in detail in Section 5.2.

3.2 Electrode analysis

Strip-type electrodes were used in the proposed 3D electric field microsensor. All the electrodes were designed into

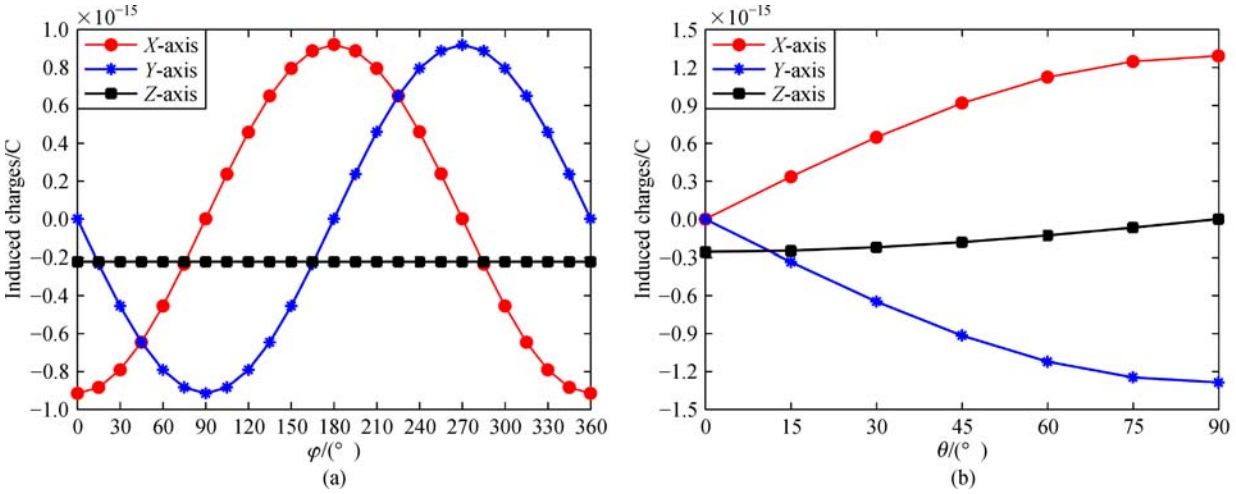

Fig. 3 Simulation results of the proposed microsensor's response to the 3D electrostatic field with different directions. (a) Induced charge along each sensing axis with respect to φ when θ is 30°; (b) induced charge along each sensing axis with respect to θ when φ is 135°

annular sector strips with large lengths and small dihedral angles on their two sidewalls. All electrodes were coaxially placed, given that the microsensor is based on in-plane rotation. For each sensing element, a pair of a sensing electrode and a shielding electrode with the same length (L), height (h), and inner radius (R) was periodically arranged, as shown in Fig. 4. w_{sn} and w_{sh} are the inner arc lengths of the sensing and shielding electrodes, respectively. The inner arc length between sensing electrode 1 and shielding electrode 1 is w_{g1}, and the inner arc length between sensing electrode 1 and shielding electrode 2 is w_{g2}. The sum of w_{g1} and w_{g2} is w_T, which remains unchanged whenever w_{g1} and w_{g2} vary due to the rotation of the shielding electrodes. Furthermore, the inner arc length between sensing electrode 1 and shielding electrode 1 is w_e when both are in the equilibrium position. These parameters determine the amount of induced charge. Therefore, an analysis should be conducted to optimize these parameters and improve the output of the proposed microsensor.

A MetalMUMPS process was implemented to fabricate the 3D electric field microsensor. This process is discussed in detail in Section 4. In accordance with the MetalMUMPS design rules, h was set to be 20 μm, and the minimum feature size of the metal layer was 8 μm. A 3D simulation was conducted to determine the remaining parameters by the FEA method. The electrode parameters were divided into two: One for the $X+$, $X-$, $Y+$, and $Y-$ sensing elements and another for the Z sensing element. These two groups of parameters should be optimized separately.

For the $X+$, $X-$, $Y+$, and $Y-$ sensing elements, L and R were preset to 1000 and 2500 μm, respectively. The presumed vibration amplitude in the inner arc was set to 10 μm. The values of w_{sn}, w_{sh}, w_T, and w_e should be determined through a simulation. Therefore, the induced charges on sensing electrode Q versus w_{g1} were simulated with different inner arc lengths of sensing electrode w_{sn}. The results are shown in Fig. 5(a). A small w_{g1} resulted in a small amount of induced charge on the sensing electrode

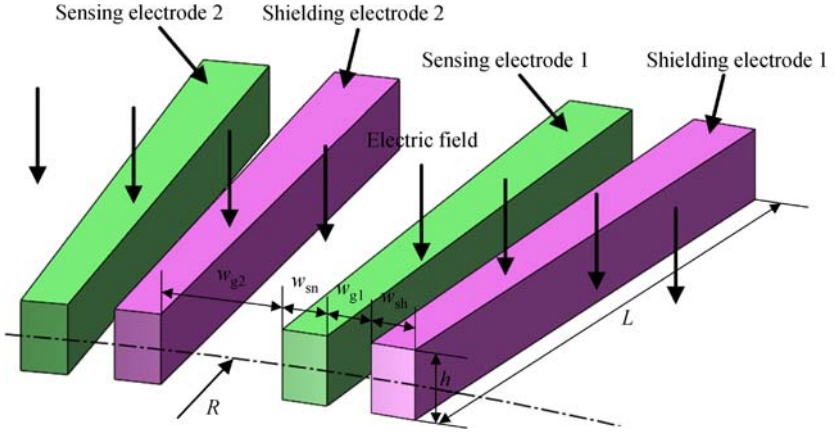

Fig. 4 Schematic of strip-type electrodes

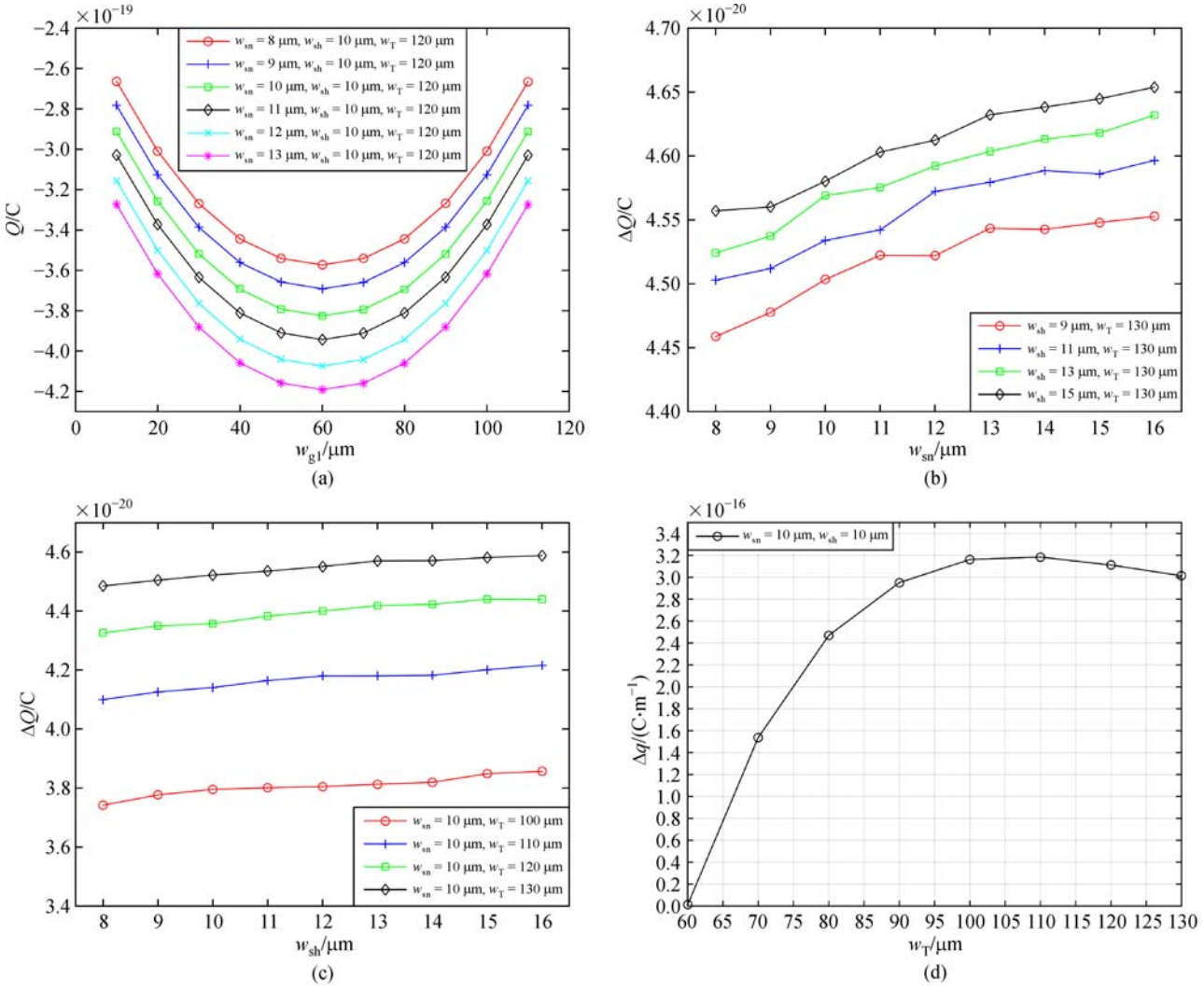

Fig. 5 Simulation results for the parameters of strip-type electrodes. (a) Induced charge on the sensing electrode versus w_{g1} with different w_{sn} values; peak-to-peak values of induced charge on the sensing electrode (b) in vibration versus w_{sn} with different w_{sh} values; (c) in vibration versus w_{g1} with different w_T values; (d) peak-to-peak value of induced charge per unit length on the sensing electrode in vibration versus w_T

but a high change rate of induced charge. Therefore, if the amplitude of the vibration is fixed, then a small w_e indicates a large peak-to-peak value of induced charge ΔQ. However, due to the impact of the squeeze-film damping factor between the sensing and shielding electrodes, both electrodes cannot be placed too close to each other when they are in the equilibrium position. In our design, for $X+$, $X-$, $Y+$, and $Y-$ sensing elements, w_e was set to 30 μm. A uniform external electric field with a strength of 1 kV/m was vertically applied to the electrodes. Moreover, the potentials of the sensing and shielding electrodes were set to zero.

To obtain an optimal w_{sn}, a simulation was conducted on the peak-to-peak values of induced charge ΔQ in the sensing electrode in vibration versus w_{sn} with different inner arc lengths of shielding electrode w_{sh}. As shown in Fig. 5(b), ΔQ increased with respect to w_{sn} with a low gradient. ΔQ increased by approximately 2% as w_{sn} increased from 8 to 16 with different w_{sh} values. This outcome suggests that w_{sn} exerts minimal influence on ΔQ. Moreover, a long w_{sn} may reduce the number of sensing units for each sensing element and consequently reduce the output of the proposed microsensor. Therefore, w_{sn} was set to 10 μm for the $X+$, $X-$, $Y+$, and $Y-$ sensing elements.

To determine w_{sh}, a simulation was conducted on the peak-to-peak values of induced charge ΔQ in the sensing electrode in vibration versus w_{sh}. According to the results shown in Fig. 5(c), ΔQ increased with increasing w_{sh}. However, ΔQ increased by less than 4% when w_{sh} increased from 8 to 16 μm with different w_{sh} values. We conclude that w_{sh} exerts minimal influence on ΔQ. A long w_{sh} results in a large mass of the resonance structure and consequently decreases the resonant frequency and output of the proposed microsensor; thus, w_{sh} was set to 10 μm.

The peak-to-peak value of induced charge per unit length, Δq, was calculated with Eq. (7) to optimize w_T conveniently.

$$\Delta q = \frac{\Delta Q}{w_{sn} + w_{sh} + w_T}. \quad (7)$$

The calculated Δq versus w_T curve is shown in Fig. 5(d). The maximum value of Δq was achieved when w_T approached 110 μm. A long w_T resulted in a small mass of the resonance structure and consequently increased resonant frequency and improved the output of the proposed microsensor. Thus, w_T was to 110 μm.

A similar simulation was performed with the FEA method for the Z sensing element. L and R were preset to 700 and 300 μm, respectively. The presumed vibration amplitude in the inner arc was set to 1.2 μm. The values of w_{sn}, w_{sh}, w_T, and w_e were determined through a simulation. The electrode parameters are listed in Table 1.

3.3 Modal simulation

In the FEA-based modal simulation, the resonant frequencies of the first six orders in the vibration mode were 838.68, 1076.0, 1076.0, 1150.7, 1454.4, and 1934.7 Hz. The in-plane rotation mode, which is the working mode of the microsensor, was the fifth order in the vibration mode with a resonant frequency of 1454.4 Hz. The remaining five vibration modes were out-of-plane vibrations. The different resonant directions ensured that the other vibration modes did not interfere with the in-plane rotation.

4 Fabrication

The sensor was fabricated through a MetalMUMPS process [26]. Figure 6 illustrates the fabrication process.

(a) A 2-μm-thick oxide, which served as an isolation

Table 1 Parameters of strip-type electrodes

Sensing element	L/μm	R/μm	h/μm	w_{sn}/μm	w_{sh}/μm	w_e/μm	w_T/μm
$X+$, $X-$, $Y+$, $Y-$	1000	2500	20	10	10	30	110
Z	700	300	20	8	8	18	60

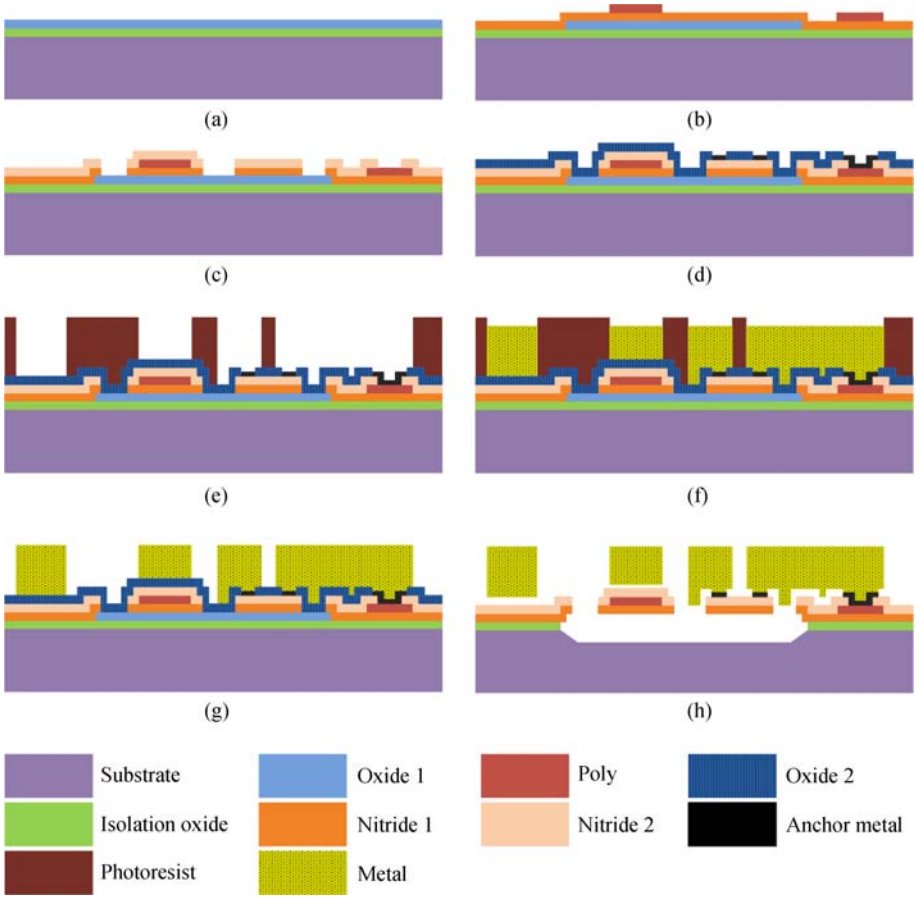

Fig. 6 Main steps of the MetalMUMPS process

layer, was grown on the surface of the starting n-type (100) silicon wafer, followed by the deposition of a 0.5-μm-thick sacrificial phosphosilicate glass (PSG) layer.

(b) The sacrificial PSG layer was patterned. Afterward, a 0.35 μm silicon layer of nitride and a 0.7 μm layer of polysilicon were deposited, and the polysilicon layer was subsequently patterned.

(c) The second silicon nitride layer was deposited and patterned as a protection material.

(d) After the deposition and patterning of the second sacrificial PSG layer, a metal layer consisting of a 10-nm-thick chrome layer and a 25-nm-thick platinum layer was deposited through a lift-off process.

(e) The wafers were coated with a thick layer of photoresist and patterned subsequently. This process formed a patterned stencil on the electroplated metal layer.

(f) A 20-μm-thick nickel layer was electroplated as the metal structure.

(g) The photoresist stencil was chemically removed.

(h) The metal structure was released by hydrogen fluoride (HF), and the remaining sacrificial layers and oxide layer over the trench areas were removed. Subsequently, the substrate layer was subjected to potassium hydroxide (KOH) etching, which formed a 25 μm groove.

Scanning electron microscope (SEM) photos of the fabricated sensor are shown in Fig. 7. The sensor size is approximately 11 mm × 11 mm.

5 Experiment and discussion

5.1 Testing system

The testing circuit of the electric field microsensor consisted of driving signal generators, I–V converters, differential amplifiers, and lock-in amplifiers, as illustrated in Fig. 8. The I–V converter converted the measured alternating current produced by the microsensor to voltage. A high-precision 1 GΩ resistor was used in the I–V converter. The differential amplifier magnified the differential output of the two opposite sensing elements by 50 times. The differential amplifier can reduce common-mode noise and increase the signal-to-noise ratio. Notably, differential amplification is inapplicable to the *Z*-axis output because only one element senses the *Z*-axis component of the electrostatic field. After differential amplification, the output voltage was connected to a METEK Model 7270 lock-in amplifier. The lock-in amplifier adopted a reference signal at the same frequency as the driving signal to eliminate superfluous information, such as the frequency and phase of the sensing signal, and obtain the amplitude of the sensing signal with respect to the electrostatic field strength. A driving signal composed of 3.5 V of AC voltage and 80 V of common direct current (DC) bias voltage was applied to excite the sensor. The resonant frequency of in-plane rotation was 1291 Hz after sweeping frequency. The simplified structure for modal simulation and squeeze-film damping accounted for the difference between the simulated resonant frequency and detected resonant frequency.

Three metal plates were parallel and equally spaced in a uniform electrostatic field. A positive voltage was applied to the upper plate, whereas a negative voltage of the same value was applied to the lower plate. The sensor with its testing circuit was fixed to the center plate by a fixture with two rotating axes. The fixture was made of Teflon, which is a widely used insulation material. By rotating the fixture on these two axes, an electrostatic field in all directions was generated. A schematic of the testing system is provided in Fig. 9.

5.2 Calibration and decoupling sensitivity matrix

Electrostatic fields parallel to the *X*-, *Y*- and *Z*-axis of the senor were applied. In each case, the outputs of the *X*-, *Y*- and *Z*-axis sensing components with respect to the electrostatic field strength ranging from 0 to 50 kV/m were all recorded for calibration, as shown in Fig. 10.

The sensitivities and linearities of the *X*-, *Y*- and *Z*-axis sensing components in the three cases are listed in Table 2. All the measured linearity errors were within 5.5%, which means that each sensing element showed a linear response to every component of the applied electrostatic field. The measured linearities indicated that the alternating current of each sensing axis could be at fA level with a 1 kV/m electric field.

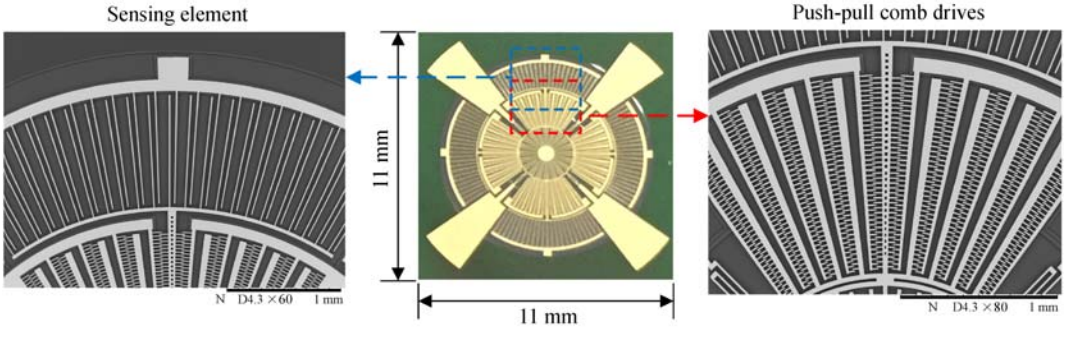

Fig. 7 SEM photos of the electric field microsensor

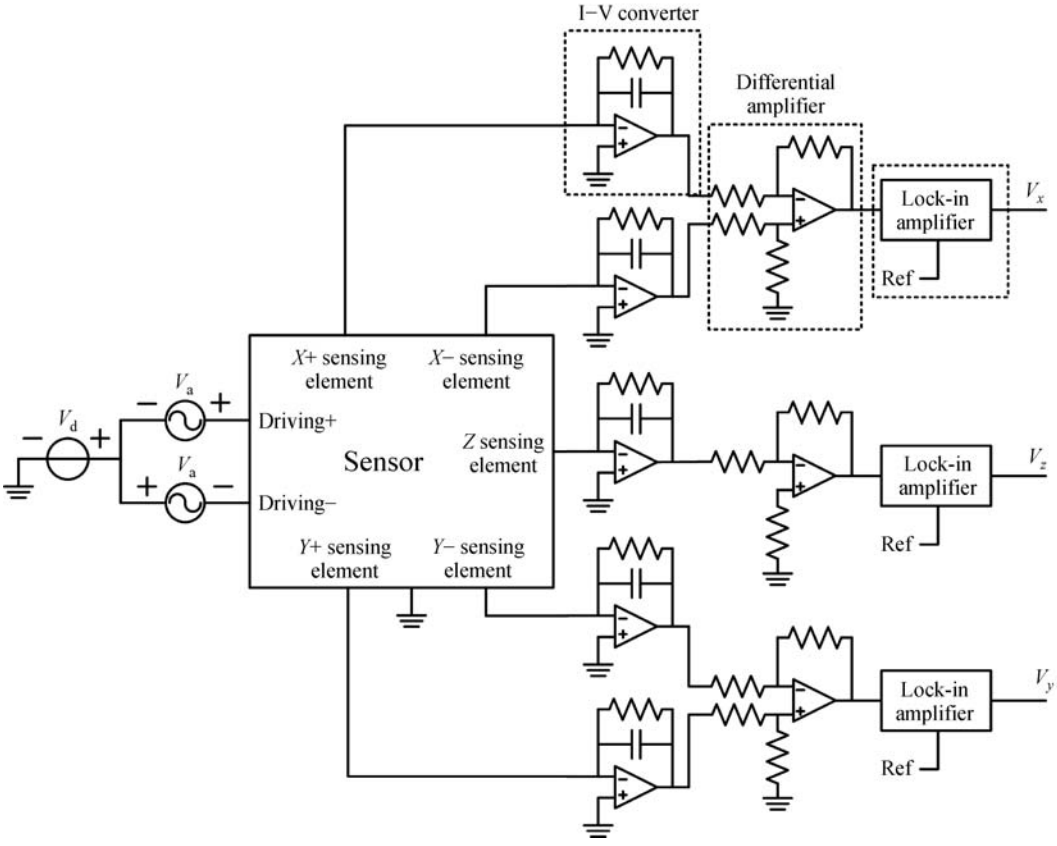

Fig. 8 Schematic of the testing circuit of the 3D electric field microsensor. V_x, V_y, and V_z are the outputs of the *X*-, *Y*-, and *Z*-axis sensing components after testing

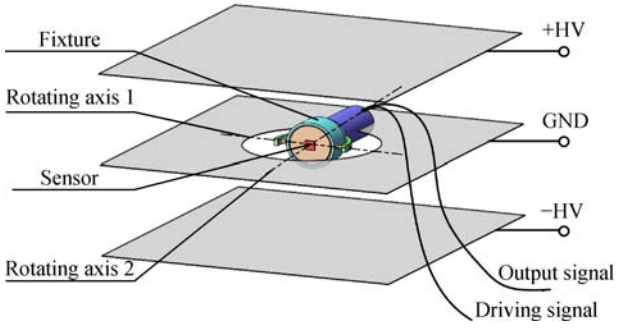

Fig. 9 Schematic of the testing system

The coupling characteristics can be described by the following matrix.

$$\begin{bmatrix} V_x - V_{x0} \\ V_y - V_{y0} \\ V_z - V_{z0} \end{bmatrix} = \begin{bmatrix} k_{xx} & k_{xy} & k_{xz} \\ k_{yx} & k_{yy} & k_{yz} \\ k_{zx} & k_{zy} & k_{zz} \end{bmatrix} \begin{bmatrix} E_x \\ E_y \\ E_z \end{bmatrix}, \quad (8)$$

where V_q is the output of the q-axis sensing component, V_{q0} is the zero output of the q-axis sensing component, and coupling sensitivity k_{qi} is the sensitivity of the q-axis sensing component to the electrostatic field in the direction i; $i = x,y,z$, and $q = x,y,z$. Therefore, the electrostatic field can be expressed as

$$\begin{bmatrix} E_x \\ E_y \\ E_z \end{bmatrix} = \begin{bmatrix} k_{xx} & k_{xy} & k_{xz} \\ k_{yx} & k_{yy} & k_{yz} \\ k_{zx} & k_{zy} & k_{zz} \end{bmatrix}^{-1} \begin{bmatrix} V_x - V_{x0} \\ V_y - V_{y0} \\ V_z - V_{z0} \end{bmatrix}. \quad (9)$$

In this study, the coupling matrix is

$$S = \begin{bmatrix} k_{xx} & k_{xy} & k_{xz} \\ k_{yx} & k_{yy} & k_{yz} \\ k_{zx} & k_{zy} & k_{zz} \end{bmatrix}^{-1} = \begin{bmatrix} 10.481 & -2.264 & -4.203 \\ -1.308 & 11.174 & -4.221 \\ -7.123 & -5.687 & 15.905 \end{bmatrix}.$$

5.3 3D electrostatic field measurement and verification

The sensor was rotated to several random angles. For each angle, electrostatic fields of 25 and 50 kV/m were applied. The outputs of the *X*-, *Y*-, and *Z*-axis sensing components were recorded to derive E_x, E_y, and E_z with a coupling

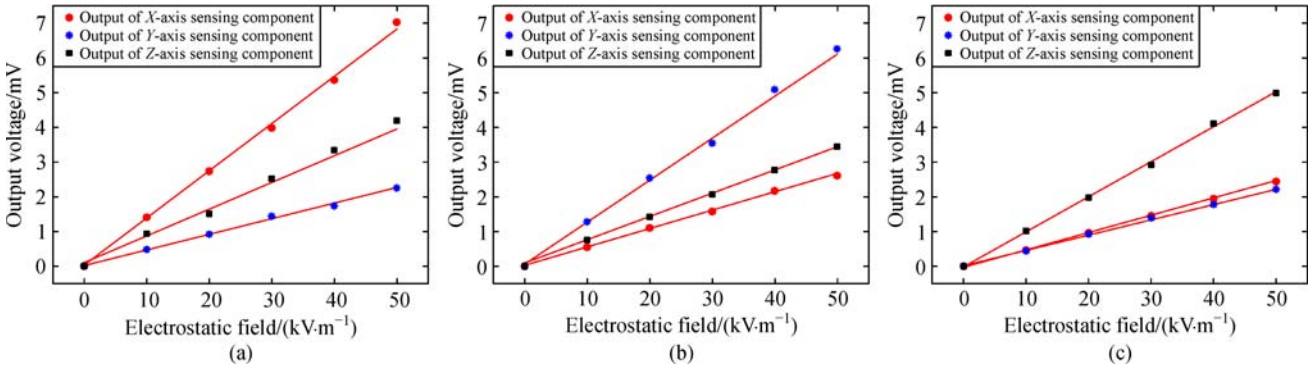

Fig. 10 Uniaxial electrostatic field calibration for the proposed sensor. (a) *X*-axis; (b) *Y*-axis; (c) *Z*-axis

Table 2 Sensitivities and linearities of the *X*-, *Y*- and *Z*-axis sensing components

Electrostatic field direction	*X*-axis sensitivity /(mV·kV^{-1}·m)	*X*-axis linearity/%	*Y*-axis sensitivity /(mV·kV^{-1}·m)	*Y*-axis linearity/%	*Z*-axis sensitivity /(mV·kV^{-1}·m)	*Z*-axis linearity/%
X direction	0.136	2.39	0.045	3.52	0.077	5.25
Y direction	0.053	2.61	0.121	3.12	0.067	2.17
Z direction	0.050	1.25	0.044	3.13	0.101	2.54

Table 3 Outputs of the sensor and calculated electric fields

Rotation angle	Applied electric field /(kV·m^{-1})	Output along the *X*-axis /mV	Output along the *Y*-axis /mV	Output along the *Z*-axis /mV	Calculated electric field /(kV·m^{-1})	Error/%
θ_1	25	2.3	2.9	1.9	27.49	9.96
θ_2	25	2.9	2.5	2.0	27.82	11.28
θ_3	25	2.5	2.2	2.4	28.51	14.04
θ_4	50	5.7	5.1	4.0	55.59	11.18
θ_5	50	4.8	5.9	3.9	56.50	13.10
θ_6	50	3.1	4.9	5.0	55.88	11.76

matrix. Moreover, the strength of the applied electrostatic field was computed with

$$E = \sqrt{E_x^2 + E_y^2 + E_z^2}. \quad (10)$$

The comparison between the calculated and applied electrostatic fields is presented in Table 3. The measurement errors were between 9.96% and 14.04%; thus, the calculated electrostatic field of the 3D electric field microsensor was consistent with the applied electrostatic field, but measurement errors still existed. These errors may be attributed to systematic errors, electric field distortion, and fabrication-induced sensor structure asymmetry.

6 Conclusions

This study presented a single-chip 3D electric field microsensor. An in-plane rotary mechanism was adopted in the microsensor to detect *X*-, *Y*-, and *Z*-axis electrostatic field components simultaneously. The proposed microsensor is compact and presents high integration. The microsensor's response to a 3D electrostatic field with different directions was investigated. The parameters of the strip-type electrodes were optimized with the FEA method. The characterization results showed that the measured linearity errors were within 5.5% in the range of 0 to 50 kV/m.

Acknowledgements This work was supported by the National Natural Science Foundation of China (Grant No. 61327810) and the National High Technology Research and Development Program of China (863 Project) (Grant No. 2015AA042602).

References

1. Maruvada P S, Dallaire R D, Pedneault R. Development of field-mill instruments for ground-level and above-ground electric field

measurement under HVDC transmission lines. IEEE Transactions on Power Apparatus and Systems, 1983, PAS-102(3): 738–744
2. Yang P, Chen B, Wen X, et al. A novel MEMS chip-based atmospheric electric field sensor for lightning hazard warning applications. In: Proceedings of IEEE Sensors. Busan: IEEE, 2015, 1–4
3. Wooi C L, Abdul-Malek Z, Ahmad N A, et al. Statistical analysis of electric field parameters for negative lightning in Malaysia. Journal of Atmospheric and Solar-Terrestrial Physics, 2016, 146: 69–80
4. Kasaba Y, Hayakawa H, Ishisaka K, et al. Evaluation of DC electric field measurement by the double probe system aboard the Geotail spacecraft. Advances in Space Research, 2006, 37(3): 604–609
5. Vaivads A, Eriksson A I, André M, et al. Low-frequency electric field and density fluctuation measurements on Solar Orbiter. Advances in Space Research, 2007, 39(9): 1502–1509
6. Pedersen A, Cattell C A, Fälthammar C G, et al. Quasistatic electric field measurements with spherical double probes on the GEOS and ISEE satellites. Space Science Reviews, 1984, 37(3–4): 269–312
7. Tant P, Bolsens B, Sels T, et al. Design and application of a field mill as a high-voltage DC meter. IEEE Transactions on Instrumentation and Measurement, 2007, 56(4): 1459–1464
8. Mathews S, Farrell G, Semenova Y. All-fiber polarimetric electric field sensing using liquid crystal infiltrated photonic crystal fibers. Sensors and Actuators A: Physical, 2011, 167(1): 54–59
9. Zhu T, Ou Z, Han M, et al. Propylene carbonate based compact fiber Mach-Zehnder interferometric electric field sensor. Journal of Lightwave Technology, 2013, 31(10): 1566–1572
10. Toney J E, Tarditi A G, Pontius P, et al. Detection of energized structures with an electro-optic electric field sensor. IEEE Sensors Journal, 2014, 14(5): 1364–1369
11. Hsu C H, Muller R S. Micromechanical electrostatic voltmeter. In: Proceedings of International Conference on Solid-State Sensors and Actuators. San Francisco: IEEE, 1991, 659–662
12. Horenstein M N, Stone P R. A micro-aperture electrostatic field mill based on MEMS technology. Journal of Electrostatics, 2001, 51–52: 515–521
13. Riehl P S, Scott K L, Muller R S, et al. Electrostatic charge and field sensors based on micromechanical resonators. Journal of Microelectromechanical Systems, 2003, 12(5): 577–589
14. Peng C, Chen X, Ye C, et al. Design and testing of a micromechanical resonant electrostatic field sensor. Journal of Micromechanics and Microengineering, 2006, 16(5): 914–919
15. Lundberg K H, Shafran J S, Kuang J, et al. A self-resonant MEMS-based electrostatic field sensor. In: Proceedings of the 2006 American Control Conference. Minneapolis: IEEE, 2006, 1221–1226
16. Chen X, Peng C, Tao H, et al. Thermally driven micro-electrostatic fieldmeter. Sensors and Actuators A: Physical, 2006, 132(2): 677–682
17. Bahreyni B, Wijeweera G, Shafai C, et al. Analysis and design of a micromachined electric-field sensor. Journal of Microelectromechanical Systems, 2008, 17(1): 31–36
18. Ghionea S, Smith G, Pulskamp J, et al. MEMS electric-field sensor with lead zirconate titanate (PZT)-actuated electrodes. In: Proceedings of 2013 IEEE Sensors. Baltimore: IEEE, 2013, 1–4
19. Yang P, Peng C, Fang D, et al. Design, fabrication and application of an SOI-based resonant electric field microsensor with coplanar comb-shaped electrodes. Journal of Micromechanics and Microengineering, 2013, 23(5): 055002
20. Wang Y, Fang D, Feng K, et al. A novel micro electric field sensor with *X*-*Y* dual axis sensitive differential structure. Sensors and Actuators A: Physical, 2015, 229: 1–7
21. Gao Z, Yu Z, Zeng R, et al. Research on measuring methods and sensors of high voltage DC electric field. In: Proceedings of International Conference on Information Science, Electronics and Electrical Engineering (ISEEE). Sapporo: IEEE, 2014, 850–854
22. Li C, Shen X, Zeng R. Optical electric-field sensor based on angular optical bias using single β-BaB_2O_4 crystal. Applied Optics, 2013, 52 (31): 7580–7585
23. Wen X, Fang D, Peng C, et al. Three dimensional electric field measurement method based on coplanar decoupling structure. In: Proceedings of 2014 IEEE Sensors. Valencia: IEEE, 2014, 582–585
24. Fang Y, Peng C, Fang D, et al. Micro 3-dimensional folding electric field sensor. Transducer and Microsystem Technologies, 2016, 35 (5): 67–73 (in Chinese)
25. Yeh J A, Chen C, Lui Y. Large rotation actuated by in-plane rotary comb-drives with serpentine spring suspension. Journal of Micromechanics and Microengineering, 2005, 15(1): 201–206
26. Allen C, Ramaswamy M, Stafford J, et al. MetalMUMPs Design Handbook, Revision 4.0, 2006